Open-loop control of a global instability in a swirling jet by harmonic forcing: a weakly non-linear analysis

Calum S. Skene,[1,*] Ubaid Ali Qadri,[2] and Peter J. Schmid[1]

[1]*Department of Mathematics, Imperial College London, London SW7 2AZ, United Kingdom*

[2]*Department of Engineering, University of Cambridge, Trumpington Street, Cambridge CB2 1PZ, United Kingdom*

(Dated: April 3, 2020)

Abstract

Highly swirling flows are often prone to precessing instabilities, with an azimuthal wavenumber of $m = -1$. We carry out a weakly non-linear analysis to determine the response behaviour of this instability to harmonic forcing. An incompressible flow is considered, where an annular inlet provides a swirling flow into a cylindrical region. For high swirl a vortex breakdown is induced, which is found to support an $m = -1$ instability. By expanding about the Reynolds number where this instability first occurs, a Stuart–Landau equation for the critical mode amplitude can be found and the effect of forcing can be assessed. Two types of forcing are considered. Firstly, a Gaussian forcing confined to the inlet nozzle is used to study $m = 0$ and $m = -1$ forcings. Secondly, optimal forcings (measured by the two-norm) with azimuthal wavenumbers in the range $-3 \leq m \leq 3$ are considered. It is found that modal stabilization is highly dependent on the azimuthal wavenumber m, which governs whether the forcing is counter or co-rotating with the direction of swirl. Counter-rotating forcings are able to stabilize the mode for a wide range of forcing frequencies, while co-rotating forcings fail to yield a stable flow. In all cases, it is the base-flow modification induced by the forced response that is the dominant underlying feature responsible for the observed stabilization. This base-flow modification seeks to reduce axial momentum near the recirculation region for co-rotating forcings, and increase it for counter-rotating forcings, thus changing the size of the recirculation bubble and producing the two distinct response behaviours.

I. INTRODUCTION

Swirling jets are commonly found in a variety of industrial applications. In gas turbine combustion, swirl injection is used to improve mixing between fuel and oxidizer and to stabilize the flame. For jets with sufficiently high swirl, vortex breakdown occurs, which is characterized by a region of recirculating fluid just downstream of the injection plane. This recirculation zone ensures a continuous supply of fresh reactants to the flame surface, thus helping to stabilize the flame [1].

Numerous experimental and numerical studies have reported the presence of a large-scale self-excited unsteady helical flow structure in such turbulent highly swirled jet configurations [2], for both reacting and non-reacting cases. This structure is commonly referred to as

* Corresponding Author: csskene@ucla.edu

the precessing vortex core (PVC). Linear stability analyses about time-averaged axisymmetric flow profiles have shown that the PVC is a manifestation of a helical global instability [3], similar to the spiral mode of vortex breakdown observed in laminar-flow configurations [4–6]. A sufficiently large region of absolute instability, around the recirculation bubble, and sometimes extending into its downstream wake, has been identified as the main condition for the onset of self-excited helical oscillations [6, 7]. Using a linear global stability analysis, the adjoint of the unstable global mode has been used to identify the wavemaker [8] – the compact region responsible for driving the self-excited oscillations. Depending on the flow configuration, the wavemaker region has been found to be located at the upstream end of the bubble [9], at the jet exit plane [10, 11], or in the wake of the bubble.

Although the origin of the PVC has become clearer now, its interaction with the flame and its effect on the performance of the combustor are not entirely transparent. Studies have shown that the PVC has an effect on flame shape and stability [12] as well as fuel-air mixing [13] in a combustor. Of particular importance in this setting is the relation of the PVC to thermo-acoustic instabilities in combustors. Heat-release fluctuations due to the PVC can interact with acoustic oscillations to both suppress and excite thermo-acoustic modes [14]. In turn, acoustic oscillations have also been shown to both suppress and excite the PVC [15].

In order to understand this complicated interaction in more detail, a reasonable first step is to understand and control the behaviour of the PVC in the absence of the flame. The response of the PVC to open-loop forcing, in particular, has received considerable attention. Recent experimental studies have looked at open-loop and feedback control of the PVC in turbulent, non-reacting configurations using harmonic forcing. For forcing with the same azimuthal wavenumber as the PVC ($m = 1$ or $m = -1$, depending on the sign convention used in the respective study), researchers observed 'lock-in' between the PVC and the forcing, accompanied by a reduction in the amplitude of the PVC [16–19]. They compared optimal actuator locations with those predicted by linear stability analysis, finding good agreement between experiments and theory [19]. For forcings with a azimuthal wavenumber different to that of the PVC ($m = 0$ or $|m| > 1$), researchers observed that the PVC could be both suppressed and excited [14–16] depending on the stability properties of the mean flow.

In addition to offering insight into the origin of the PVC, linear stability analysis can also provide insight into the control of the PVC. The adjoint global mode provides linear receptivity information – it identifies the regions of the flow that are most receptive to

harmonic forcing at the frequency of the global mode [7]. For passive control strategies, the adjoint mode can then be used within a Lagrangian optimization framework to identify locations where a steady volume force or wall blowing/suction strategy will be most effective in controlling the growth rate and frequency of the global mode [20]. In the context of swirling jets, these techniques have been used to study the control of the helical global mode in laminar [21–23] and, more recently, turbulent regimes [11, 19]. These studies have found that regions upstream of the bubble and in the inlet nozzle are highly receptive to open-loop forcing and passive control efforts.

Although these approaches are highly insightful, they fail to predict the effect of forcing with a *different* wavenumber and frequency to that of the global mode, as this requires non-linearity to be taken into account. For globally unstable flows near the threshold of instability, a multiple-scale analysis can be used to derive a Stuart-Landau equation that accounts for the saturation of the amplitude of the linear global mode [24]. This approach was demonstrated in the case of flow over a cavity and flow behind a cylinder and was subsequently used to model the interaction between the helical and double-helical modes of a swirling flow [25]. More recently, this weakly non-linear analysis has been extended to account for the effect of small-amplitude harmonic forcing on the amplitude and frequency of the unstable global mode [26]. For the case of cavity flow, it was possible to completely suppress the self-excited oscillations using high-frequency forcing.

In this study, we investigate whether this weakly non-linear approach can be applied to study the control of self-excited helical oscillations in a uniform-density incompressible swirling jet. We extend the framework of Sipp [26] to consider the effect of harmonic forcing over a range of azimuthal wavenumbers. For each wavenumber, we determine the range of frequencies over which the helical mode is stabilized and destabilized, the type of forcing that is most effective, and the physical mechanisms that facilitate the control of the global mode.

II. MATHEMATICAL FORMULATION

A. Governing Equations

We consider a jet exiting from an annular inlet into a cylindrical domain. The flow geometry is shown in figure 1. Region 0 consists of the inlet annulus which has length

$x_{\text{inlet}} = 5$, inner and outer radii $r_{\text{in}} = 3/11$ and $r_{\text{out}} = 1$, respectively, with the central rod protruding into region 1 by an amount $x_{\text{rod}} = 2/11$. The size of the cylindrical region is set by $r_{\text{outlet}} = 3$ and $x_{\text{outlet}} = 40$. We use a cylindrical coordinate system and work entirely in non-dimensional variables which are summarized in table I.

Non-dimensional variable	Definition	Non-dimensional constant	Definition
Length	$\boldsymbol{x} = \dfrac{\hat{\boldsymbol{x}}}{L}$	Reynolds number	$Re = \dfrac{\rho_0 U r_{\text{out}}}{\mu}$
Velocity	$\boldsymbol{u} = \dfrac{\hat{\boldsymbol{u}}}{U}$	Swirl number	$S = \dfrac{\int_{r_{\text{in}}}^{r_{\text{out}}} rwur \text{ dr}}{(r_{\text{out}} - r_{\text{in}}) \int_{r_{\text{in}}}^{r_{\text{out}}} u^2 r \text{ dr}}$
Pressure	$P = \dfrac{\hat{P}}{\rho_0 U^2}$		
Time	$t = \dfrac{\hat{t}}{L/U}$		

TABLE I. Definitions of the non-dimensional parameters and variables. The reference velocity U is the maximum longitudinal velocity at the inlet, and the length L is the outer radius of the inlet annulus. μ is the dynamic viscosity. The radii r_{in} and $r_{\text{out}}$are the non-dimensional inner and outer radii of the annulus, respectively. The swirl number is calculated at $x = x_{\text{inlet}}$.

The motion of the fluid is governed by the forced constant-density incompressible Navier–Stokes equations, written in non-dimensional form as

$$\nabla \cdot \boldsymbol{u} = 0, \tag{1}$$

$$\frac{\partial \boldsymbol{u}}{\partial t} + \nabla \cdot (\boldsymbol{u} \otimes \boldsymbol{u}) = -\nabla P + \frac{1}{Re} \nabla \cdot \boldsymbol{\tau} + \boldsymbol{f}', \tag{2}$$

where the velocity vector $\boldsymbol{u} \equiv (u, v, w)^T$ contains the axial, radial, and azimuthal velocities, respectively, $\boldsymbol{\tau}$ denotes the viscous stress tensor, and $\boldsymbol{f}'$ represents the forcing vector.

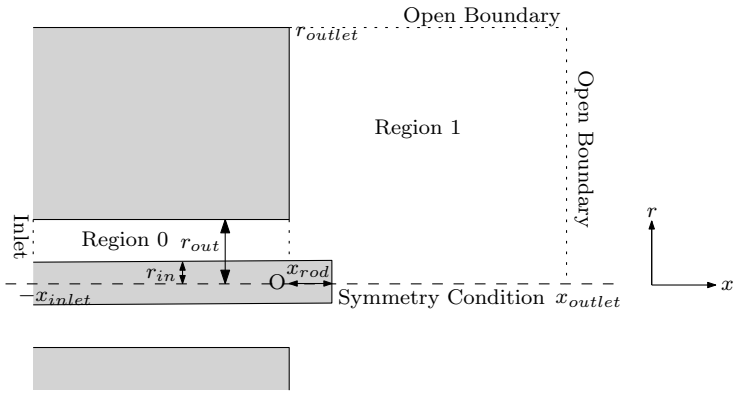

FIG. 1. Sketch of the computational domain for the simulations. The domain size is given by x_{inlet}, x_{outlet} and r_{outlet}. We show the reflection of the domain across the line $r = 0$, but the flow is not solved there; instead, a symmetry condition is applied.

B. Weakly nonlinear formulation

We follow the approach of Sipp [26] to obtain the amplitude equation for our unstable mode in the presence of harmonic forcing. An outline of the analysis is presented here, with further details being provided in appendix A. For ease of notation we rewrite the governing equations (1-2) as

$$\boldsymbol{B}\frac{\partial \boldsymbol{q}}{\partial t} = \boldsymbol{\mathcal{R}}(\boldsymbol{q}) + (\boldsymbol{C}F'\boldsymbol{f}(x,r)e^{i\omega_f t + im_f\theta} + \text{c.c}), \tag{3}$$

where we have specified that the forcing has azimuthal wavenumber m_f, temporal frequency ω_f and amplitude F'. The state vector is specified as $\boldsymbol{q} = (\boldsymbol{u}, P)^T$, and the matrix $\boldsymbol{B}$ enforces that the time derivative only applies to the momentum equations and the relevant velocity components. Likewise, the matrix $\boldsymbol{C}$ implies that the forcing $\boldsymbol{f} = (f_x, f_r, f_\theta)^T$ only drives the momentum equations.

From previous studies and preliminary investigations, we know that the flow is steady and axisymmetric below a critical Reynolds number, which we denote Re_c. We consider the asymptotic expansion of the flow about this critical point by writing $Re^{-1} = Re_c^{-1} - \delta'$, where $\delta' = \epsilon^2\delta$ for small ϵ, and δ is a user-specified parameter proportional to the distance from criticality. For the case of non-resonant forcing, we use the scaling $F' = \epsilon F$ and seek solutions for the flow in increasing powers of ϵ

$$\begin{aligned}\boldsymbol{q}(t,x,r,\theta) = \boldsymbol{q}_0(x,r) &+ \epsilon\left[A\boldsymbol{q}_A e^{-i\theta+i\omega_c t} + F\boldsymbol{q}_F e^{im_f\theta+i\omega_f t} + \text{c.c.}\right] \\ &+ \epsilon^2\Big[\boldsymbol{q}_\delta + \boldsymbol{q}_{A\bar{A}} + \boldsymbol{q}_{F\bar{F}} + \big(\boldsymbol{q}_{AA}e^{-2i\theta+2i\omega_c t} + \boldsymbol{q}_{AF}e^{i(m_f-1)\theta+i(\omega_c+\omega_f)t} \\ &+ \boldsymbol{q}_{A\bar{F}}e^{i(-m_f-1)\theta+i(\omega_c-\omega_f)t} + F^2\boldsymbol{q}_{FF}e^{2im_f\theta+2i\omega_f t} + \text{c.c.}\big)\Big] + \text{h.o.t.},\end{aligned} \tag{4}$$

where $\boldsymbol{q}_0$ is a steady axisymmetric solution to the governing equations at $Re = Re_c$, $\boldsymbol{q}_A$ is the linear global mode with amplitude A, azimuthal wavenumber $m = -1$ and frequency ω_c, $\boldsymbol{q}_F$ is the linear forced response with amplitude F, and the other terms are the base flow modifications and harmonic terms arising from the interaction between the global mode and the forced response and their conjugates. By substituting (4) into (3) and equating terms in various orders of ϵ, we obtain a series of linear equations that can be solved to obtain the flow responses and interactions at the different orders. Here, using the adjoint global mode $\boldsymbol{q}_A^\dagger$ to satisfy compatibility conditions, at third order, we can obtain a scalar equation for the complex amplitude of the unstable mode A

$$\frac{\mathrm{d}A}{\mathrm{d}T} = \left(\eta\delta - |F|^2\mu\right) A - \nu A|A|^2. \tag{5}$$

Here $T = \epsilon^2 t$ is the slow time scale on which the amplitude evolves, η and ν are complex coefficients that control the linear growth rate and saturation of the global mode to a limit cycle in the absence of forcing, and $\mu := \mu(\omega_f)$ is a complex coefficient that controls the effect of the forcing on the growth rate of the mode, with $\Re(\mu) > 0$ leading to a more stable flow and $\Re(\mu) < 0$ leading to a more unstable flow.

Although complete stabilization of the mode may be possible, the forcing energy to accomplish this goal may be prohibitively high. In this case, we can still utilize a forcing to control the limit-cycle behaviour. As shown by Sipp [26], the limit-cycle amplitude is directly proportional to the growth rate, and the change in the limit-cycle frequency due to the forcing is controlled by the parameter

$$\gamma(\omega_f) = \Re(\mu(\omega_f)) \left(-\frac{\Im(\mu(\omega_f))}{\Re(\mu(\omega_f))} + \frac{\Im(\eta)}{\Re(\eta)} \right). \tag{6}$$

This leads to two possible control strategies considered by Sipp [26]. Either one reduces the growth rate or limit cycle amplitude (through μ), or one shifts the limit-cycle frequency to a less dangerous one (through γ). In our work, we will focus mainly on the first (stabilization) strategy.

It is important to note that the amplitude equation obtained at third order is not valid if terms with wavenumber $m = -1$ and frequency $\omega = \omega_c$ occur at lower orders. For our study this means that the three cases of $m_f = 0$ and $\omega_f = 0$, $m_f = -2$ and $\omega_f = 2\omega_c$, and $m_f = -1$ and $\omega_c = \omega_f$ cannot be studied using the above formulation. Using alternative asymptotic scalings [26] leads to different amplitude equations for these cases (see appendix). In the first case, steady forcing can directly influence the growth rate with a forcing amplitude an

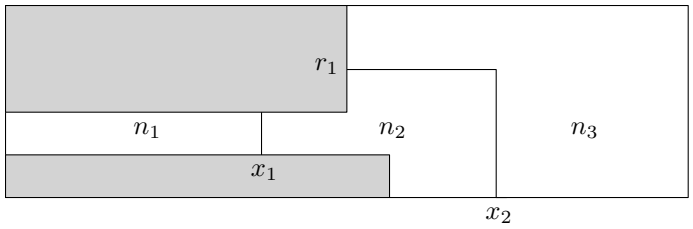

FIG. 2. The computational grid consists of three regions of different mesh densities, with $x_1 = -0.5$, $r_1 = 1.5$ and $x_2 = 3$, and mesh densities $n_1 = 12n_r$, $n_2 = 20n_r$, and $n_3 = 8n_r$, where $n_r = 1.5$ is a mesh-refinement parameter.

order of magnitude smaller than for non-resonant harmonic forcing, and with a stabilising or destabilising effect depending on the sign of F. In the latter two cases, although resonant forcing provides a cheap way to alter the frequency of the flow, direct manipulation of the eigenvalue is not possible. For this reason, we will not consider these cases in more detail in this present study.

C. Numerical Implementation

We use a numerical code based on the FEMSTAB package developed by Garnaud *et al.* [27, 28], that has been modified by Qadri and Schmid [29] in a recent weakly non-linear study. In this code, the governing equations (1)-(2) are multiplied by r, and the weak form of the resulting equations is then solved in FREEFEM++ [30] using the finite-element method. Taylor-Hood elements (*P2*-elements for the velocity components and *P1*-elements for the pressure) are used. The linearised stiffness matrix is found by explicitly linearising equations (1)-(2) about a given base flow and by proceeding in the same manner as in the non-linear case. Access to the adjoint matrix is obtained by transposing the linearised matrix.

The numerical domain is discretised on an unstructured mesh, comprising three regions with different mesh densities, as shown in figure 2. We found that $n_r = 1.5$ is sufficient for all eigenvalues and Stuart-Landau coefficients to converge to mesh-independent quantities. (see appendix B).

No-slip boundary conditions are used for the velocity at the walls and Neumann conditions are applied at the lateral and outlet boundaries. The inflow condition is a velocity profile with a chosen swirl number as defined by the formula given in table I. Additionally, we need

$\lvert m\rvert$	single-valued	multi-valued
0	Neumann	Dirichlet
1	Dirichlet	Neumann
≥ 2	Dirichlet	Dirichlet

TABLE II. The centreline boundary conditions for single-valued and multi-valued quantities for different azimuthal wavenumbers m.

to apply boundary conditions at $r = 0$ to close the problem. These take the form of either a homogeneous Dirichlet or homogeneous Neumann boundary condition, and they depend on the mode being solved for and if the variable is single-valued or multi-valued at $r = 0$ [31]. The type of boundary condition for each mode is shown in table II, where the pressure P and axial velocity u are single-valued quantities, whereas the radial and azimuthal velocities, v and w, respectively, are multi-valued.

We obtain a steady base flow $\boldsymbol{q}_0$ using a Newton–Raphson method, by starting at a low Reynolds number and using the converged base flow as an initial guess for a higher Reynolds number. Iterations are continued until the desired critical Reynolds number Re_c is obtained. This procedure is possible because the flow is stable to axisymmetric disturbances. The linearised (A5) and adjoint (A19) eigenvalue problems are solved using the shift-invert Arnoldi method as implemented in the integrated ARPACK package. Matrix inversions, that are required for the solution of the forced response (A6) as well as the harmonic and base-flow modifications in equations (A9)-(A14), are handled using the MUMPS package. A more detailed description of the numerical implementation can be found in the thesis by Skene [32].

III. RESULTS

A. No added forcing

We first consider the flow with no harmonic driving, i.e., $F = 0$. This will provide a baseline against which we can measure the effect of forcing. We consider a swirling jet with swirl number $S = 0.87$. As the Reynolds number is increased, a vortex breakdown bubble forms on the jet axis. At $Re = Re_c = 295.95$, we find that the steady base flow is unstable to perturbations with $m = -1$. Figure 3 shows the steady base flow that is obtained at the

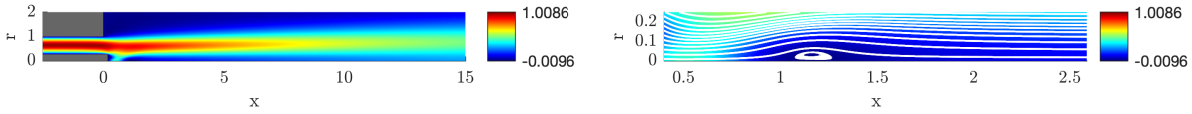

(a) The steady axisymmetric base-flow.

(b) A zoomed plot of the recirculation bubble with streamlines superimposed.

FIG. 3. The axial velocity component of the steady axisymmetric base flow $\boldsymbol{q}_0$ for $S = 0.87$ at the threshold of instability, $\mathrm{Re}_c = 295.95$.

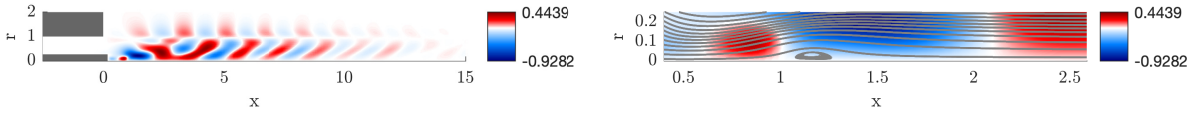

(a) $\Re(u_A)$

(b) Zoom of $\Re(u_A)$ with streamlines superimposed.

FIG. 4. The axial velocity component of the unstable mode for the base flow in figure 3.

critical Reynolds number. The vortex breakdown bubble is situated around one jet diameter downstream of the inlet plane and is significantly smaller than the bubble seen in previous studies featuring the Grabowski profile [4].

For this base flow, we find, for $m = -1$, a marginally unstable linear global mode with a frequency $\omega_c \approx 2.10$. The axial velocity component of this mode is shown in figure 4. The real and imaginary parts of the mode are a quarter of a wavelength out of phase, have large

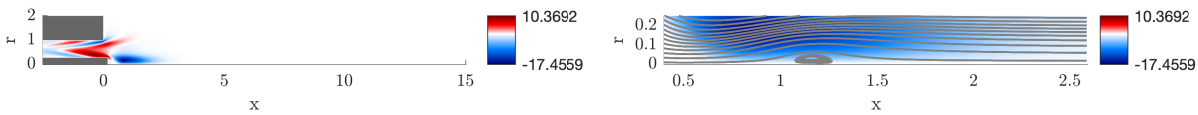

(a) $\Re(u_A^\dagger)$

(b) Zoom of $\Re(u_A^\dagger)$ with streamlines superimposed.

FIG. 5. The axial velocity component of the unstable adjoint mode for the base flow in figure 3.

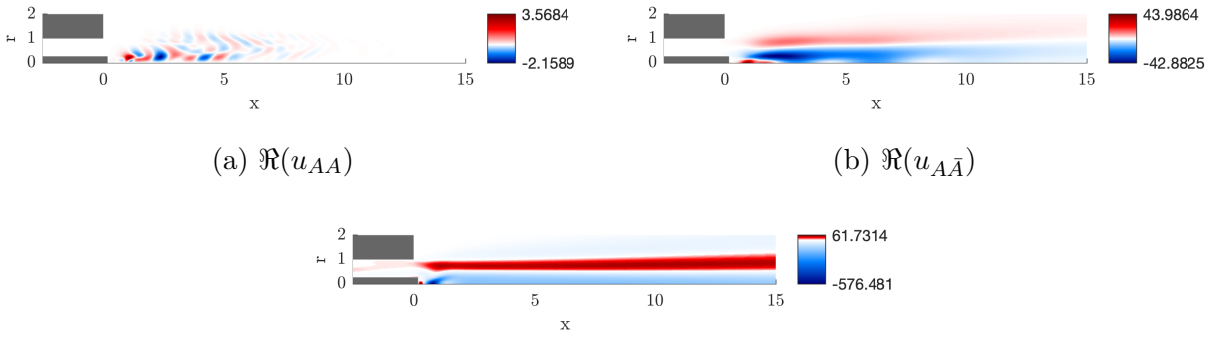

(a) $\Re(u_{AA})$ (b) $\Re(u_{A\bar{A}})$

(c) $\Re(u_{\delta})$

FIG. 6. The axial velocity component of the harmonics and base-flow modifications caused by the unstable mode in figure 4.

magnitudes in the vicinity of the breakdown bubble and decay further downstream in its wake. This is similar to the behaviour seen by Qadri *et al.* [9], who studied spiral vortex breakdown in a flow featuring the Grabowski profile. In their work, they considered the use of the adjoint mode to obtain structural sensitivity information, and we can use similar ideas to better understand the adjoint mode, shown in figure 5.

The adjoint mode consists of two types of structures. Firstly, there are a series of tilted streaks in the inlet nozzle and near the jet exit-plane. This structure is associated with the Orr-mechanism and is due to the strong non-normality of the swirling jet. It is similar to structures seen in uniform-density and low-density jets. Secondly, there is a region of high amplitude near the vortex breakdown bubble. The corresponding structures are associated with the helical mode of vortex breakdown and are similar to structures seen in spiral vortex breakdown based on the Grabowski profile [9, 25]. In practice, the unstable mode is highly sensitive to changes in the regions where the adjoint mode has high amplitude. As an inner product with the adjoint eigenvector is used to reduce our original vector equation to a scalar one, this means that only terms that overlap significantly with the adjoint eigenvector and hence lie inside this highly sensitive region will be effective at changing the behaviour of the global mode.

Using the obtained direct mode we are able to calculate its harmonic and base-flow modification. Figure 6a shows that the harmonic has a large magnitude near the jet centreline up to about five jet diameters downstream of the inlet plane. The base-flow modification,

shown in figure 6b, has a much larger magnitude near the recirculation bubble and in the inner shear layer downstream. We observe that the base flow modification is such that it increases the axial velocity in the vicinity of the recirculation bubble, decreases the velocity in the inner shear layer downstream, and weakly increases the axial velocity in the outer shear layer. This has the effect of smearing out the shear and increasing the spreading rate of the jet. Together, these two terms (and particularly the base-flow modification) are responsible for the saturation of the instability to form a limit cycle. The initial growth of the instability stems from the viscous term at second order shown in figure 6c, as well as the third-order viscous term from the unstable mode which is not shown. Figure 6c shows that the viscous term at second order induces a large negative axial velocity near the recirculation bubble. Physically, this corresponds to an increase in the size of the recirculation bubble as the Reynolds number is increased. By combining these fields with the adjoint mode we obtain the parameters $\eta = 267.73 - 7.73i$, and $\nu = 32.3 + 33.2i$. As $\Re(\eta) > 0$ we recover that the flow will be unstable for $\mathrm{Re} > \mathrm{Re}_c$, as expected. We also have $\Re(\nu) > 0$, which means that the non-linearities will saturate the instability into a limit cycle.

B. Gaussian forcing

In this section we consider the effect of Gaussian forcing in the inlet nozzle. Specifically, we show results for axisymmetric ($m_f = 0$) and helical ($m_f = -1$) forcing. For each of these cases, the forcing is taken to be a simple Gaussian in the axial velocity component, hence the forcing can be written as

$$\boldsymbol{f} = \left(G \exp\left(-\frac{(x+1)^2 + (r-0.5)^2}{0.1^2} \right), 0, 0 \right)^T, \tag{7}$$

with G a constant chosen so that the forcing has unit norm $\langle \boldsymbol{f}, \boldsymbol{f} \rangle = 1$. As shown in section II B, the ability of the forcing to manipulate the mode is determined by the real part of μ. Therefore, by calculating this parameter for a range of forcing frequencies, we can assess the stabilizing behaviour of the Gaussian forcing as a function of the forcing frequency. Besides the real part of μ, another parameter of interest is the gain of the forced linear response. This is a measure of the linear amplification of the forcing by the flow and is calculated as the ratio of the norm of the response over the norm of the forcing, according to

$$\sigma = \frac{\|\boldsymbol{u}_F\|}{\|\boldsymbol{f}\|} = \langle \boldsymbol{u}_F, \boldsymbol{u}_F \rangle. \tag{8}$$

By calculating the gain for each frequency, we can see how responsive the base flow is to particular forcing frequencies. The real part of μ and the corresponding linear gains are shown in figure 7 for non-resonant forcing frequencies. We have removed points near the invalid frequencies to stress that the amplitude equation (5) is not valid in the vicinity of these frequencies.

Figure 7c shows that forcing with $m_f = 0$ is destabilizing for all frequencies, except for low values where it is marginally stabilizing. Conversely, Figure 7d shows that forcing with $m_f = -1$ is stabilizing for all frequencies, except for small ranges below the sub-harmonic ($\omega_c/2$) and harmonic (ω_c), respectively. The most effective forcing frequency for stabilizing the global mode (apart from just below the critical frequency) is $\omega_f \approx 1.7$, which is located near a local peak in the frequency-response curve, around $\omega_f \approx 1.8$. Figure 7b shows that there is a particularly large frequency response at $\omega_f \approx \omega_c$. This is simply due to resonance with the global mode.

The forcing also has an effect on the frequency of the limit cycle. Figure 7e shows that forcing with $m_f = 0$ decreases the frequency of the limit cycle, except for low values of ω_f where it increases the frequency of the limit cycle (while also having a stabilizing influence). Conversely, figure 7f shows that forcing with $m_f = -1$ increases the frequency of the limit cycle in the range $\omega_c/2 < \omega_f < \omega_c$ and decreases the limit-cycle frequency outside this range. It is also interesting to note that there is a slight asymmetry in the receptivity to forcing for ω_f just above and just below the natural frequency of the global mode. Forcing just below the natural frequency is more effective. This has also been observed in experiments of forced turbulent swirling jets [19]. It is worth noting however that figure 7 is technically valid for very small forcing amplitudes. It does not capture 'lock-in' behaviour that is observed for larger forcing amplitudes, as has been observed in a variety of nonlinear systems.

To understand the effects of the forcing, we will analyze the most stabilizing frequency for $m_f = -1$ (which is $\omega_f \approx 1.7$ away from the harmonic) and the most destabilizing frequency for $m_f = 0$ (which is $\omega_f \approx 1.3$) in more detail. Figures 8 and 9 show the forced response, harmonics and base-flow modifications due to these two types of forcing. We can see that there are fundamental differences between the two cases. The $m_f = 0$ response manifests itself in a series of perturbations confined to the inner shear layer far downstream of the inlet. On the other hand, the $m_f = -1$ response shows far more activity near the core of the swirling jet and closer to the vortex breakdown bubble and inlet plane. These responses translate into differences in the harmonics, with the $u_{A\bar{F}}$ harmonic being further downstream

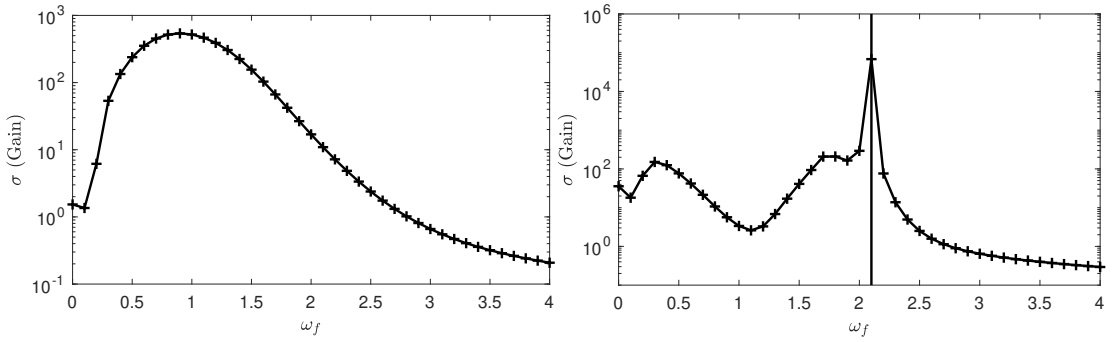

(a) The gain of the linear frequency response

(b) The gain of the linear frequency response for $m_f = -1$

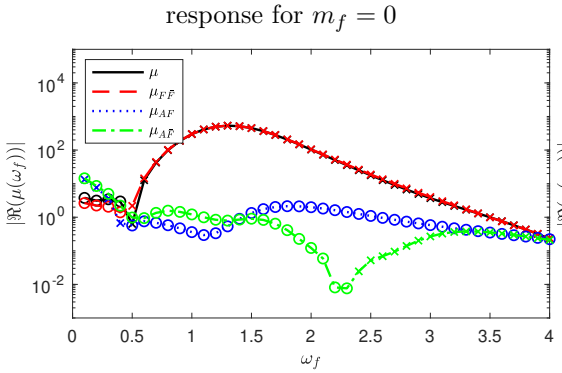

(c) The weakly non-linear coefficient μ for $m_f = 0$

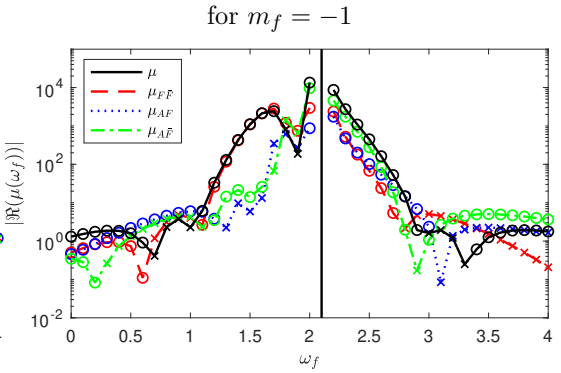

(d) The weakly non-linear coefficient μ for $m_f = -1$

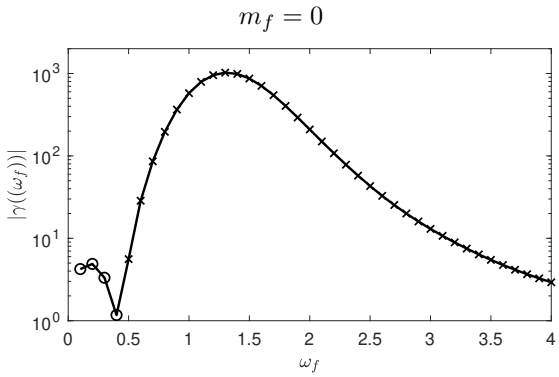

(e) The frequency shift term γ for $m_f = 0$

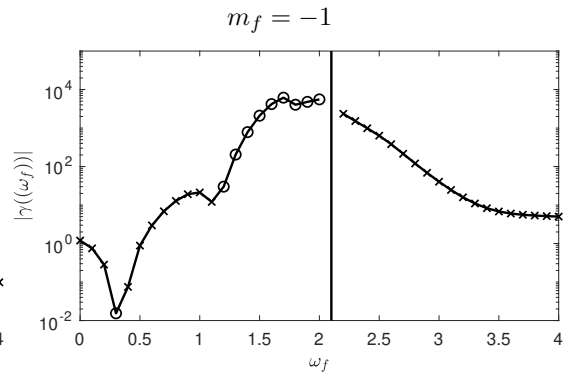

(f) The frequency shift term γ for $m_f = -1$

FIG. 7. The gain, real part of μ and γ are shown for a range of frequencies. Calculated frequencies are shown as plus-symbols in the gain plots, and crosses and circles in the μ and γ plots. Circles denote a positive sign for μ (stabilizing) or γ, and crosses denote a negative sign. The vertical solid black lines shows the resonant frequency ω_c, for which, in the case of $m_f = -1$, the amplitude equation is not valid.

for $m_f = 0$ forcing than for $m_f = -1$ forcing, which is also situated closer to the centreline. This behaviour is also demonstrated by the u_{AF} harmonic. The base-flow modifications $u_{F\bar{F}}$ show opposite signs near the recirculation bubble – $m_f = 0$ forcing reduces the axial velocity while $m_f = -1$ forcing increases the axial velocity.

To extend this analysis, we proceed by recognizing that the vector field μ has three distinct contributions. Equation (A16) shows that $\boldsymbol{\mu}$ is determined as a sum of vector fields according to

$$\boldsymbol{\mu}_{F\bar{F}} = \boldsymbol{u}_A \cdot \nabla_0 \boldsymbol{u}_{F\bar{F}} + \boldsymbol{u}_{F\bar{F}} \cdot \nabla_{-1} \boldsymbol{u}_A, \tag{9}$$

$$\boldsymbol{\mu}_{AF} = \bar{\boldsymbol{u}}_F \cdot \nabla_{m_f-1} \boldsymbol{u}_{AF} + \boldsymbol{u}_{AF} \cdot \nabla_{-m_f} \bar{\boldsymbol{u}}_F, \tag{10}$$

$$\boldsymbol{\mu}_{A\bar{F}} = \boldsymbol{u}_A \cdot \nabla_{-(m_f+1)} \boldsymbol{u}_{A\bar{F}} + \boldsymbol{u}_{A\bar{F}} \cdot \nabla_{m_f} \boldsymbol{u}_F, \tag{11}$$

and hence we can write $\mu = \mu_{F\bar{F}} + \mu_{AF} + \mu_{A\bar{F}}$, where each contribution stems from its corresponding vector field. By examining the magnitude of these contributions, shown by additional lines in figures 7c and 7d, we find that $\mu_{F\bar{F}}$ is dominant for $m_f = 0$ forcing and is mostly dominant for $m_f = -1$ as well. For $m_f = -1$ forcing at frequencies $\omega_f \geq 1.8$, the interactions of the unstable mode with the forced response and its conjugate become more important. However, for our sub-critical optimal frequency of $\omega = 1.7$, the base-flow modification term is still dominant. As $\mu_{F\bar{F}}$ is calculated from the interaction of the unstable mode with the base-flow modification caused by the forced response, we conclude that nonlinear base-flow modifications play a key role in controlling the growth rate of the global mode at non-resonant frequencies.

It is not the base-flow modification directly that is responsible for the control of the global-mode amplitude, but rather the interaction between the base-flow modification and the unstable mode. This interaction is precisely the vector field $\boldsymbol{\mu}_{F\bar{F}}$. We use this field when we calculate μ, through the term $\mu_{F\bar{F}} = \langle \boldsymbol{u}^\dagger, \boldsymbol{\mu}_{F\bar{F}} \rangle$. If, instead of taking the inner product we take the element-wise, or Hadamard, product $\boldsymbol{\mu}^I_{F\bar{F}} = \bar{\boldsymbol{u}}^\dagger \circ \boldsymbol{C}^T \boldsymbol{W} \boldsymbol{C} \boldsymbol{\mu}_{F\bar{F}}$, we obtain a structure whose elements sum to $\mu_{F\bar{F}}$. Through this structure we can thus determine which areas of the flow, modified by the interaction of the base-flow correction with the unstable mode, lead to either stabilization or destabilization. Both the interaction term $\boldsymbol{\mu}_{F\bar{F}}$ and structural term $\boldsymbol{\mu}^I_{F\bar{F}}$ are shown in figures 10 and 11 for the two types of forcing considered thus far.

We can see from figure 10a that the axial component of the interaction consists of a localised bubble with positive values near the inner shear layer and recirculation bubble.

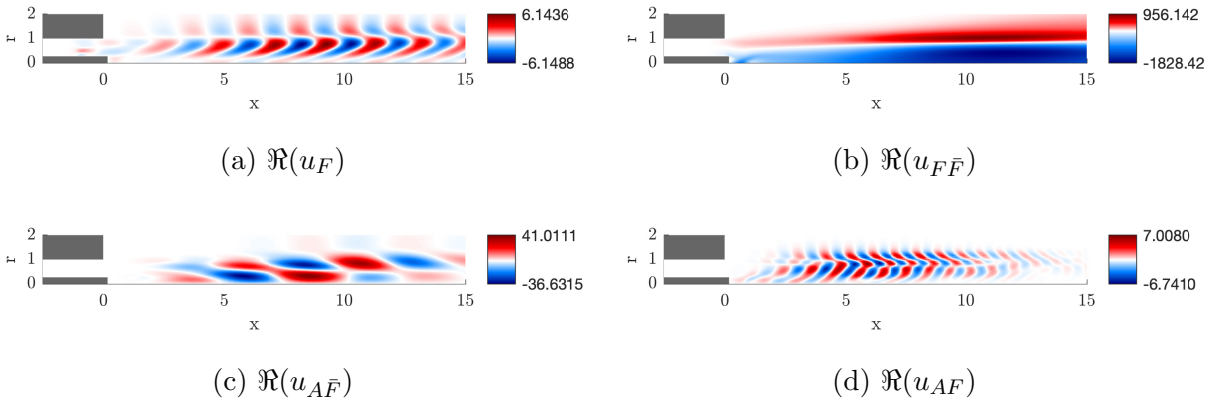

(a) $\Re(u_F)$ (b) $\Re(u_{F\bar{F}})$

(c) $\Re(u_{A\bar{F}})$ (d) $\Re(u_{AF})$

FIG. 8. Axial velocity components of the forced response, mean-flow modification, and harmonics for forcing with $m_f = 0$ and $\omega_f = 1.3$.

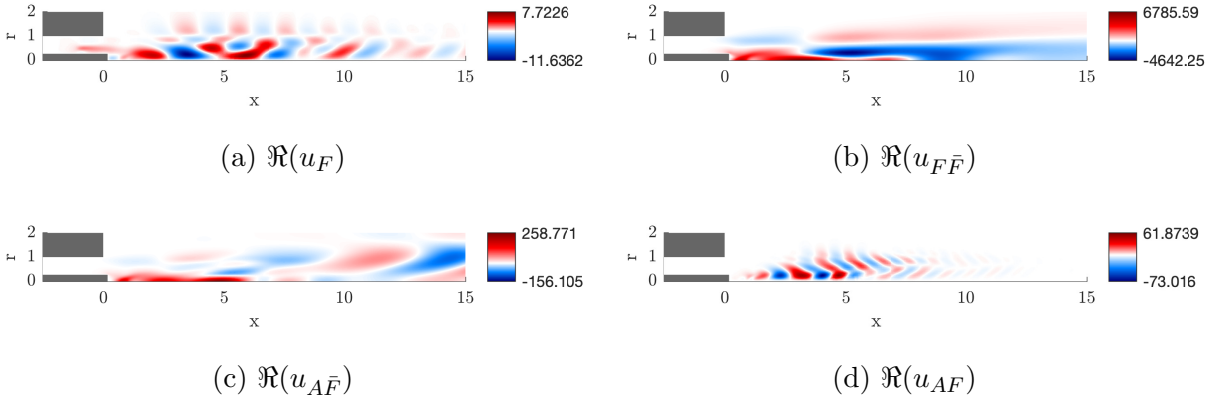

(a) $\Re(u_F)$ (b) $\Re(u_{F\bar{F}})$

(c) $\Re(u_{A\bar{F}})$ (d) $\Re(u_{AF})$

FIG. 9. Axial velocity components of the forced response, mean-flow modification, and harmonics for forcing with $m_f = -1$ and $\omega_f = 1.7$.

The structural vector in figure 10b then shows that it is almost entirely this bubble that contributes to the term $\mu_{F\bar{F}}$. Moreover, the figure shows a negative contribution in the shear layer upstream of the bubble, with a further positive contribution downstream in the shear layer around the bubble. As the negative contribution outranks the positive one, we get an overall destabilizing effect. For $m_f = -1$ we can see from figure 11 that the interaction term also contains a bubble in the same location, but this time it is negative. This leads to a similar structural vector, however, in this case the positive part outweighs the negative,

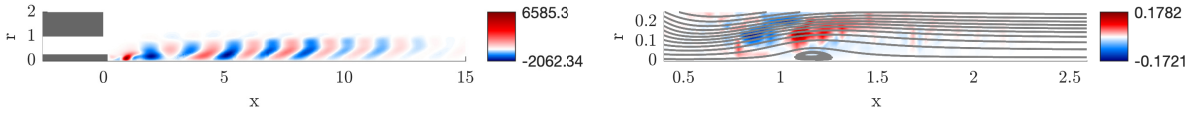

(a) $\Re(\mu_{u,F\bar{F}})$

(b) $\Re(\mu^I_{u,F\bar{F}})$ zoomed in with streamlines superimposed

FIG. 10. Weakly nonlinear interaction terms due to base-flow modifications arising from the Gaussian forcing with $m_f = 0$ at $\omega_f = 1.3$ (axial velocity components shown).

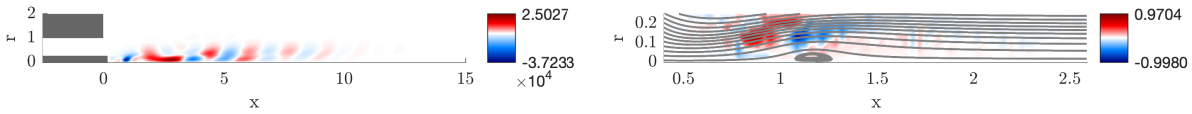

(a) $\Re(\mu_{u,F\bar{F}})$.

(b) $\Re(\mu^I_{u,F\bar{F}})$ zoomed in with streamlines superimposed

FIG. 11. Weakly nonlinear interaction terms due to base-flow modifications arising from the Gaussian forcing with $m_f = -1$ at $\omega_f = 1.7$ (axial velocity components shown).

ultimately leading to stabilization. In particular, these figures highlight that the effect of the two modes is nearly identical in location, albeit with a different sign.

The opposite effect of forcing with $m_f = 0$ and $m_f = -1$ can be more clearly traced back to the base-flow modification (figures 8 and 9). We see that the $m_f = -1$ forcing gives an increased longitudinal velocity in the core of the jet, upstream of the vortex breakdown bubble and in its wake. This weakens both the shear and the recirculation and suppresses the instability mechanism which, for spiral vortex breakdown, is a combination of a shear-driven (Kelvin-Helmholtz) and a centrifugal instability [9, 10]. Conversely, for $m_f = 0$ forcing, the base-flow modification acts to reduce the velocity in the jet core, and to increase it in the outer shear layer. This change tends to increase the shear as well as the recirculation, and thus strengthens the identified instability mechanisms.

As described in section II B and appendix A, even though the amplitude equation is not valid for $m_f = 0$, and $\omega_f = 0$ for the $\mathcal{O}(\epsilon)$ forcing considered so far, it is possible to get a valid

amplitude equation by forcing at $\mathcal{O}(\epsilon^2)$. In this case, it is a direct interaction between the forced response and the unstable mode at $\mathcal{O}(\epsilon^3)$ that gives rise to a change in the eigenvalue as shown by equation (A24). In the case of our Gaussian forcing this produces a value of $\mu = -0.12 + 6.15i$ showing that we can obtain a marginally stabilizing or destabilizing effect. Even though this effect is less when compared to other forcing frequencies, it should be noted that the overall cost to achieve this manipulation of the instability is less, since the forcing is one power of ϵ smaller.

C. Optimal forcing of all wavenumbers

We now extend our analysis to consider a variety of wavenumbers and forcing structures. As we have seen in section III B, the ability of the forcing to manipulate the amplitude of the mode is related to – but not entirely due to – the magnitude of the forced response. Hence, in order to make a fair comparison between azimuthal modes and frequencies we will proceed by considering only the optimal forcing, i.e. choosing $\mathbf{f}$ by solving

$$\underset{\boldsymbol{f}}{\operatorname{argmax}} \frac{\|\boldsymbol{u}_F\|}{\|\boldsymbol{f}\|} = \underset{\boldsymbol{f}}{\operatorname{argmax}} \frac{\|\boldsymbol{C}^T(i\boldsymbol{B}\omega_f - \boldsymbol{L}_{m_f})^{-1}\boldsymbol{C}\boldsymbol{f}\|}{\|\boldsymbol{f}\|}. \tag{12}$$

This can be solved using singular value decomposition (SVD) directly in FREEFEM++ following the approach of Sipp and Marquet [33]. Furthermore, the first order accurate formula

$$\frac{\partial \sigma}{\partial \omega} = \sigma^2 \Im[\langle \boldsymbol{f}, \boldsymbol{u}_F \rangle], \tag{13}$$

is used to allow us to interpolate between gains using cubic-Hermite splines [34].

We will only consider positive forcing frequencies. This is possible since $\bar{\boldsymbol{L}}_m = \boldsymbol{L}_{-m}$ which in turn implies that the response $\boldsymbol{q}_F$ to frequency ω_f for wavenumber m_f produces the response $\bar{\boldsymbol{q}}_F$ for frequency $-\omega_f$ and wavenumber $-m_f$. Hence, by considering positive frequencies ω_f we allow the wavenumber m to control the direction of the forcing in the θ-direction. This means that positive values of m_f lead to forcing in the direction of the mean swirl, while negative values of m_f yield forcings counter to the mean swirl.

Figures 12a and 12b show the optimal gains of the forced response for positive and negative wavenumbers, respectively. We show wavenumbers up to $m = 3$ as this is the highest amplified. For positive wavenumbers, the optimal gains for each frequency increase with increasing wavenumber. Meanwhile, the frequency at which perturbations are most linearly amplified decreases with increasing wavenumber. For forcing with $m_f = 2$ and

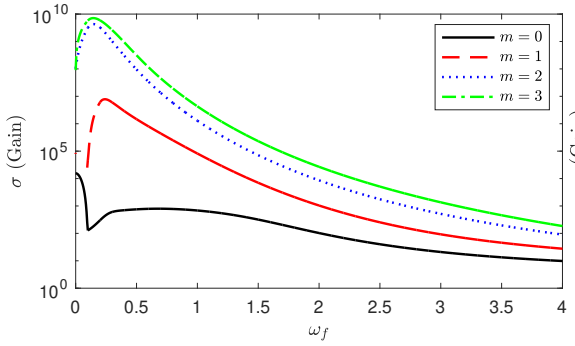

(a) Optimal gain of the linear frequency response for positive wavenumbers.

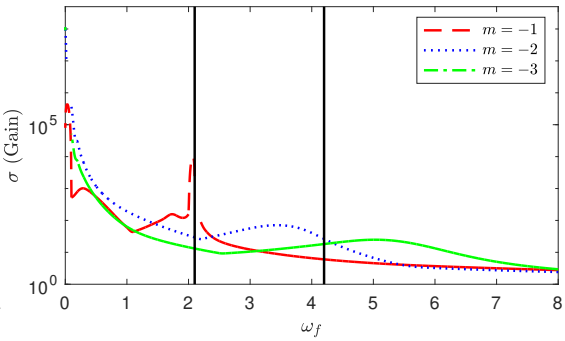

(b) Optimal gain of the linear frequency response for negative wavenumbers.

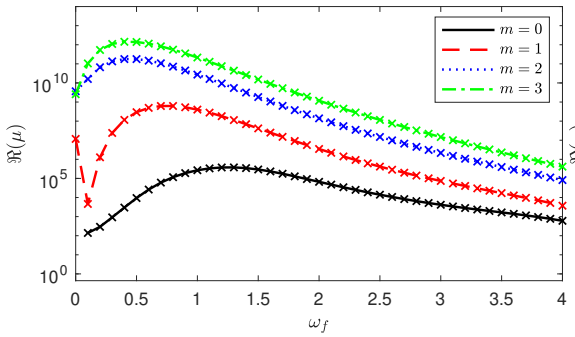

(c) The optimal weakly nonlinear coefficient μ for positive wavenumbers.

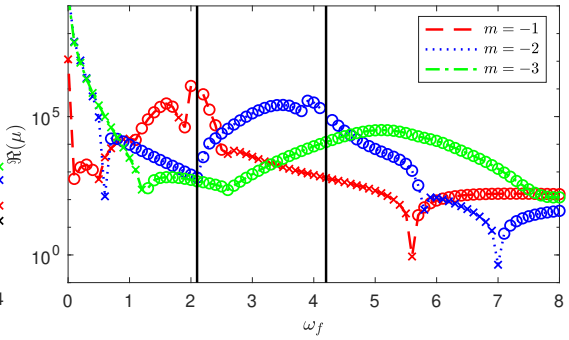

(d) The optimal weakly nonlinear coefficient μ for negative wavenumbers.

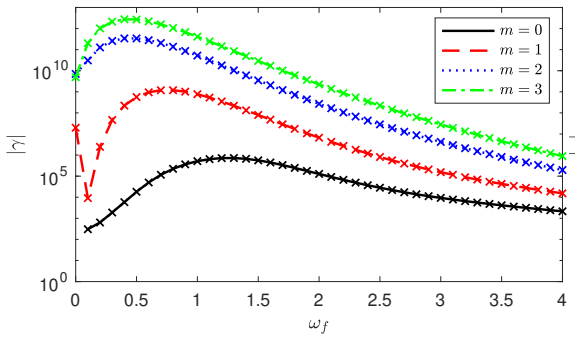

(e) The optimal frequency shift parameter γ for positive wavenumbers.

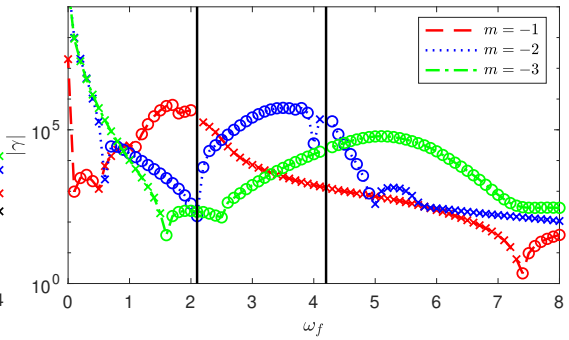

(f) The optimal frequency shift parameter γ for negative wavenumbers.

FIG. 12. The optimal gains of the forced linear response for positive and negative wavenumbers, along with the values of the coefficients μ and γ. The vertical lines show the resonant frequencies ω_c and $2\omega_c$ where the amplitude equation may not valid depending on the wavenumber of the forcing. Circles are used to show that $\mu, \gamma > 0$, while crosses indicate that $\mu, \gamma < 0$.

$m_f = 3$, we see linear optimal gains of up to 10^{10} in magnitude. Whilst this may seem unobservably high, it is important to remember that this is a linear phenomenon. The substantial gains here should not be interpreted as a unit-norm forcing leading to an $\mathcal{O}(10^{10})$ response, but instead as a forcing of $\mathcal{O}(10^{-10})$ that would lead to an $\mathcal{O}(1)$ response. In other words, the substantial gain should be interpreted in terms of a considerable sensitivity to harmonic forcing. This large gain is a direct consequence of the strong non-normality of jet flows and has been observed in non-swirling jets as well [27]. Perturbations with positive wavenumbers are greatly amplified in the flow – for these wavenumbers, the flow is strongly convectively unstable. Under this interpretation, we see that the flow is particularly sensitive to forcings in the direction of the swirl.

For negative wavenumbers, we find that forcing with $m_f = -1$ is the most linearly amplified in the vicinity of the global-mode frequency, with the shape of the gain-frequency curve closely mirroring the relationship obtained in figure 7b. The higher magnitude of the gains shown in figure 12b is simply due to the forcing structure being chosen optimally. Forcing with $m_f = -2$ has the highest linear optimal gain for low frequencies but also shows an increased gain around $\omega_f \approx 3.9$, while forcing with $m_f = -3$ has an increased gain around $\omega_f \approx 5.1$.

From figure 12c, we see that forcing with positive wavenumbers and axisymmetric forcing is destabilizing across the entire range of frequencies considered. At the same time, forcing with these wavenumbers decreases the frequency of the unstable mode. In contrast (see figure 12d), we see that forcing with negative wavenumbers can be stabilizing across a range of forcing frequencies. Harmonic driving with $m_f = -1$ remains the most stabilizing wavenumber to force with in the vicinity of the global-mode frequency. For higher values of ω_f, forcing with $m_f = -2$ and $m_f = -3$ show large stabilizing effects at $\omega_f \approx 3.9$ and $\omega_f \approx 5.1$, respectively. For $m_f = -3$, this strong stabilizing influence is due to the base-flow modification caused by the large forced response at this frequency as shown in figure 12b. For $m_f = 2$, the mechanism is slightly more complicated, and the stabilizing effect is due to the base-flow modification caused by the large forced response around this frequency and also the interaction between the harmonic $\boldsymbol{u}_{A\bar{F}}$ (or its associated conjugate) and the unstable mode. The harmonic is particularly effective at this frequency because it has wavenumber $m_f = 1$ and temporal frequency ω close to ω_c (or, equivalently, $m_f = -1$ and ω close to ω_c), and hence, is close to resonance with the unstable mode. Indeed, it is this harmonic that causes the amplitude equation to become invalid when $\omega_f = 2\omega_c$, as in this case the

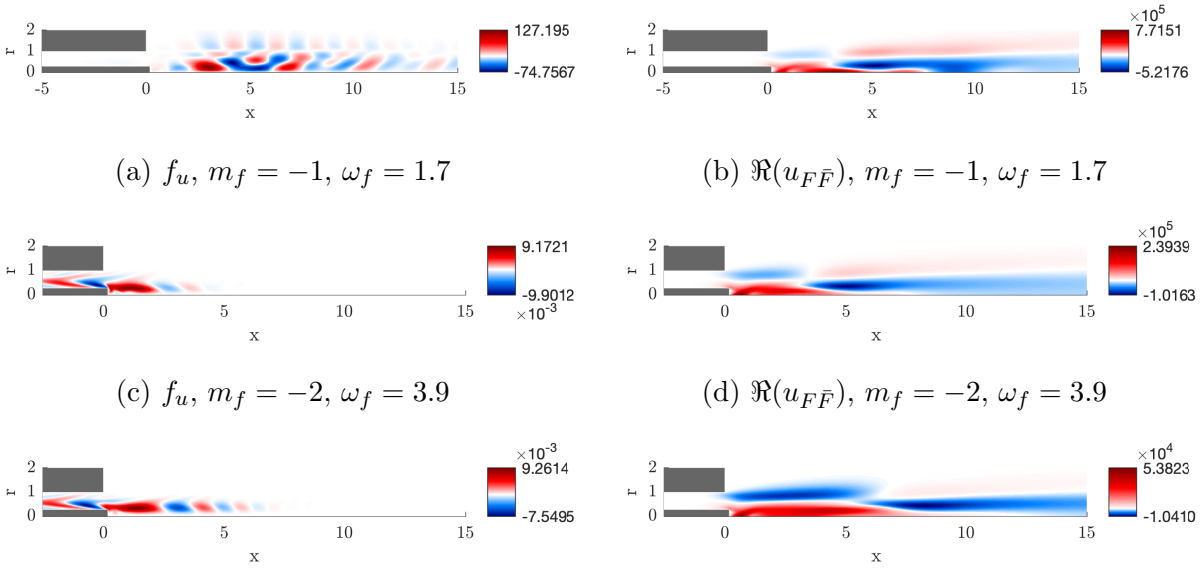

(a) f_u, $m_f = -1$, $\omega_f = 1.7$ (b) $\Re(u_{F\bar{F}})$, $m_f = -1$, $\omega_f = 1.7$

(c) f_u, $m_f = -2$, $\omega_f = 3.9$ (d) $\Re(u_{F\bar{F}})$, $m_f = -2$, $\omega_f = 3.9$

(e) f_u, $m_f = -3$, $\omega_f = 5.1$ (f) $\Re(u_{F\bar{F}})$, $m_f = -3$, $\omega_f = 5.1$

FIG. 13. Axial velocity components of the optimal forcing and induced base-flow modification for most stabilizing frequencies for negative wavenumbers.

harmonic has a frequency exactly equal to the critical value.

The effect of the optimal forcing on the limit-cycle frequencies is shown in figure 12f. No clear physical mechanism can be proposed for the increase or decrease in the limit-cycle frequency. Of particular interest, however, is the asymmetry observed in the effect of forcing on either side of the harmonics. Around the first harmonic ($\omega_f = \omega_c$), forcing with $m_f = -1$ is more effective just below the corresponding frequency value, while forcing with $m_f = -2$ is more effective just above the harmonic. Around the second harmonic ($\omega_f = 2\omega_c$), forcing with $m_f = -1$ does not exhibit any preferential amplification (because no resonant structures are induced), but forcing with $m_f = -2$ is more effective just below the second harmonic.

Figure 13 shows the optimal forcings and base-flow modifications for negative wavenumbers. For $m_f = -1$ the optimal forcing shows a series of slanted structures in the inlet nozzle and a positive body force in the axial direction above the recirculation region (see figure 13a). This induces a base-flow modification, shown in figure 13b, that is similar to that obtained with Gaussian forcing. From this we can conclude that, in the case of optimal forcing, we stabilize the mode using the same physical mechanism as discussed in the previ-

ous section. However, by choosing the forcing optimally we invoke a large gain in the driven response, which increases the magnitude of the stabilizing effect. For higher wavenumbers, the optimal forcings show similar features – a series of slanted structures in the inlet nozzle and some body forcing in the vicinity of the recirculation bubble. The base-flow modification also shares the same features: an increase in the velocity in the core of the jet.

This particular structure for the optimal forcing, with fluid elements angled against the mean shear, points towards an Orr-related mechanism providing the optimal gain. This amplification mechanism is not uncommon and has been reported in jets by Garnaud *et al.* [28], in reactive jets by Skene and Schmid [34], and in boundary-layer flow by Sipp and Marquet [33], among others. The selection of this mechanism is also reflected in the adjoint mode (figure 5a), which exhibits a slanted structure in the inlet nozzle, highlighting the sensitivity in this region. Therefore, if the Orr mechanism is invoked by forcing against the mean shear in the inlet, we can obtain stabilization with $m_f = -1$ forcings at smaller driving amplitudes.

For all wavenumbers considered, the stabilization or destabilization can be linked to the sign of the base-flow modification, as introduced in section III B. Figure 14 shows the base-flow modifications that lead to the largest effect, for all azimuthal wavenumbers considered. It is clear that forcing in the direction of the swirl (or in an axisymmetric manner) destabilizes the flow by inducing base-flow modifications that decrease the axial velocity in the recirculation region, whereas forcing counter to the swirl stabilizes the flow by inducing base-flow modifications that increase the axial velocity in the recirculation region.

Similarly to the case of Gaussian forcing, we can still consider the effect of $m_f = \omega_f = 0$ forcing using an $\mathcal{O}(\epsilon^2)$ forcing. In this case we obtain μ through equation (A24) to be $\mu = -234.63 + 400.81i$, again showing that stabilization or destabilization is possible in the case of optimal forcing. The contrast in effect of optimal forcing for $m_f = 0$ at $\omega_f = 0$ with the destabilizing behaviour seen for all other forcing frequencies can be attributed to the fact that it is not the base-flow modification induced by the forced response, but the forced response itself that provides the observed mode manipulation in this case.

IV. VERIFICATION

We now proceed to verify our analysis using a self-consistent approach. In the previous sections it was determined that base-flow modifications arising from the forced response

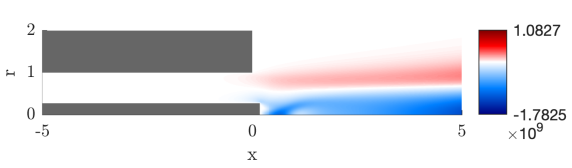

(a) $\Re(u_{F\bar{F}})$, $m_f = 1$, $\omega_f = 0.8$

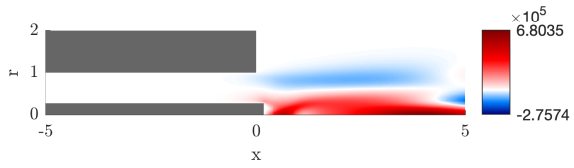

(b) $\Re(u_{F\bar{F}})$, $m_f = -1$, $\omega_f = 1.6$

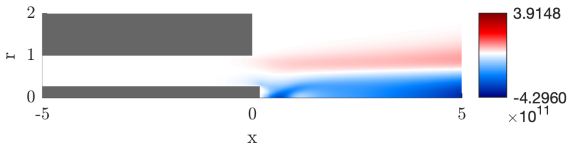

(c) $\Re(u_{F\bar{F}})$, $m_f = 2$, $\omega_f = 0.4$

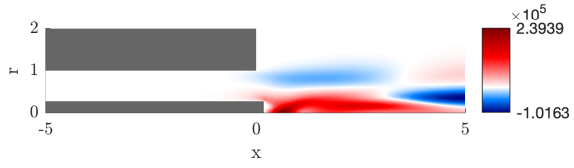

(d) $\Re(u_{F\bar{F}})$, $m_f = -2$, $\omega_f = 3.9$

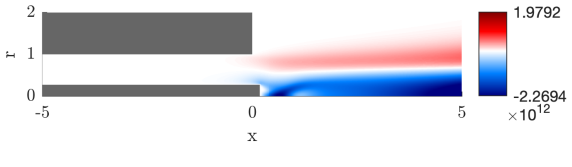

(e) $\Re(u_{F\bar{F}})$, $m_f = 3$, $\omega_f = 0.4$

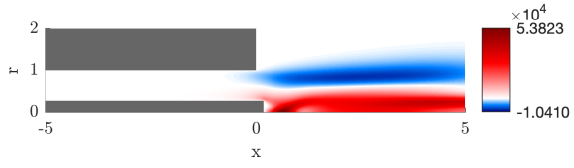

(f) $\Re(u_{F\bar{F}})$, $m_f = -3$, $\omega_f = 5.1$

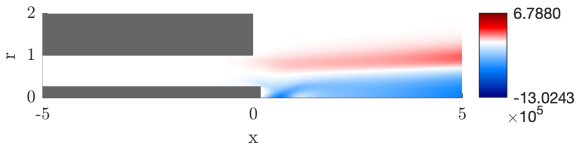

(g) $\Re(u_{F\bar{F}})$, $m_f = 0$, $\omega_f = 1.3$

FIG. 14. Base-flow modifications for various azimuthal wavenumbers, showing the longitudinal velocity components in each case.

constitute the dominant terms that cause either stabilization or destabilization. Therefore, to validate the predictions made by the $\boldsymbol{\mu}_{F\bar{F}}$ part of the amplitude equation, we verify that the eigenvalues, obtained from the original base-flow with a small amount of the base-flow modification superimposed, are modified in the manner predicted by our analysis. As $\boldsymbol{\mu}_{F\bar{F}} \approx \boldsymbol{\mu}$, this verification, even though neglecting the cumulative effect of the harmonics, provides a valuable check of our analysis. This verification is carried out below for the two

ϵ_b	$m_f = 0,\ \omega_f = 1.3$	$m_f = -1,\ \omega_f = 1.7$
0	$-4.72 \times 10^{-6} + 2.096i$	$-4.72 \times 10^{-6} + 2.096i$
10^{-7}	$1.02 \times 10^{-4} + 2.095i$	$-5.73 \times 10^{-4} + 2.097i$
10^{-6}	$1.06 \times 10^{-3} + 2.093i$	$-5.76 \times 10^{-3} + 2.108i$
10^{-5}	$1.05 \times 10^{-2} + 2.075i$	$-6.70 \times 10^{-2} + 2.233i$

TABLE III. The modified eigenvalue, computed with various amounts of the base-flow modifications added.

cases studied in section III B.

For $m_f = -1$, and $\omega_f = 1.7$, we obtain a parameter value $\mu = 2421.4 - 6229.1i$. As the real part is positive, we conclude that adding the base-flow modification to the base-equilibrium should make the modified eigenvalue more stable, i.e., we expect to observe a more negative real part. Similarly, since the imaginary part of μ is negative, we infer that the frequency of the eigenvalue should increase, and therefore the imaginary part of the eigenvalue should be greater than ω_c. Likewise, for $m_f = 0$ and $\omega_f = 1.3$, we calculate $\mu = -533.0 + 1040.0i$. Consequently, the modified eigenvalue in this case should have a larger real and smaller imaginary part.

Table III shows the eigenvalues that are obtained when the base-flow is modified according to

$$\boldsymbol{q}_b = \boldsymbol{q}_0 + \epsilon_b \boldsymbol{q}_{F\bar{F}}. \tag{14}$$

We can see that, for $m_f = -1$, increasing the amount of superimposed base-flow modification decreases the real part of the eigenvalue, whilst increasing its imaginary part. Conversely, for the $m_f = 0$ mode, augmenting the amount of base-flow modification increases the real part and decreases the imaginary part. This is precisely what is predicted by the amplitude equation, verifying that our weakly non-linear analysis is self-consistent and correctly captures first-order changes to the stability of the flow due to non-linearities.

V. CONCLUSIONS

Precessing motion is a common occurrence in flows subject to high mean-flow swirl. It manifests itself as an instability of an axisymmetric base flow to perturbations with an azimuthal wavenumber of $m = -1$. The response of this inherent instability to time-

harmonic forcing has been studied in this article, in particular its nonlinear saturation into finite-amplitude limit cycles. A weakly nonlinear analysis, anchored around the critical Reynolds number for the onset of this stability, provides an evolution equation for the slowly evolving amplitude of the precessing instability structure.

First, a user-defined harmonic body forcing in the inlet nozzle has been studied, covering the axisymmetric and $m = -1$ case, after which the body forcing has been chosen to optimize the frequency response gain or transfer function norm. In the latter cases, azimuthal wavenumbers covering the range $-3 \leq m \leq 3$ have been assessed. In both cases, the sign of the azimuthal wavenumber has a critical influence on nonlinear stabilization by harmonic forcing. Broadly speaking, forcings that run counter to the mean-flow swirl achieve stabilization of the otherwise unstable configuration (at least for the bulk of investigated forcing frequencies), while co-rotating forcing failed to produce the same modal stabilization. While theoretically the mechanisms underlying this stability modification could arise (i) from a nonlinear interaction with induced higher harmonics or (ii) a modification of the mean-flow at criticality and its subsequent interaction with the primary disturbance, it is the latter possibility that dominates the stabilization process. A more detailed analysis of this dominant mechanism revealed that it is linked to a change in length of the prevalent vortex-breakdown bubble: for co-rotating forcing, the recirculation bubble length is increased yielding a more unstable flow configuration, while for counter-rotating forcing, the shortened recirculation bubble accommodates a more stable perturbation dynamics across a substantial range of forcing frequencies. This mean-flow modification by harmonic forcing has been identified as the key characteristic of the two distinguishable response behaviors.

ACKNOWLEDGMENTS

We acknowledge the EPSRC for the PhD scholarship on which this research was conducted. UAQ would like to thank the Leverhulme Trust and Isaac Newton Trust for the Early Career Fellowship that allowed this work to be completed.

Appendix A: Weakly non-linear analysis

1. Non-resonant forcing

We begin with the governing equations written in the form

$$\boldsymbol{B}\frac{\partial \boldsymbol{q}}{\partial t} = \boldsymbol{\mathcal{R}}(\boldsymbol{q}) + (\boldsymbol{C}F'\boldsymbol{f}(x,r)e^{i\omega_f t + im_f\theta} + \text{c.c}). \tag{A1}$$

This formulation allows us to separate the Navier–Stokes operator into $\boldsymbol{\mathcal{R}}(\boldsymbol{q}) = \boldsymbol{\mathcal{N}}(\boldsymbol{q}) - \epsilon^2\delta\boldsymbol{C}\nabla\cdot\boldsymbol{\tau}$, where $\boldsymbol{\mathcal{N}}(\cdot)$ denotes the standard Navier–Stokes operator at the threshold of instability at $Re = Re_c$. By letting $\mathcal{O}(\epsilon)$ be the order at which the linear dynamics, and hence the unstable mode, are found, and similarly by choosing the forcing amplitude $F' = \epsilon F$ such that the forced response is described as a linear effect, we seek a solution of the form

$$\boldsymbol{q}(t,x,r,\theta) = \boldsymbol{q}_0(x,r) + \epsilon\boldsymbol{q}_1(t,x,r,\theta) + \epsilon^2\boldsymbol{q}_2(t,x,r,\theta) + \text{higher order terms.} \tag{A2}$$

Substituting this expression into the governing equations and separating out powers in ϵ produces, at $\mathcal{O}(\epsilon^0)$,

$$\boldsymbol{\mathcal{N}}(\boldsymbol{q}_0) = 0. \tag{A3}$$

This establishes $\boldsymbol{q}_0$ as a steady solution of equation (A1).

For $Re > Re_c$, the flow is globally unstable to a mode with azimuthal wavenumber $m = -1$. This is a co-rotating but counter-winding helical mode. To account for the response to forcing, we follow the scalings used by Sipp [26] and set the forcing to be of order ϵ. Hence, the first-order solution is a superposition of the marginally unstable mode and the response to this forcing, and can be written as

$$\boldsymbol{q}_1(t,x,r,\theta) = \underbrace{A\boldsymbol{q}_A(x,r)e^{-i\theta+i\omega_c t}}_{\text{m=-1 instability}} + \underbrace{F\boldsymbol{q}_F(x,r)e^{im_f\theta+i\omega_f t}}_{m=m_f \text{ forced response}} + \text{c.c}, \tag{A4}$$

where ω_c is the frequency of the unstable helical mode and A and F denote the amplitudes of the unstable mode and the forced response, respectively. Based on linear superposition, we can solve for $\boldsymbol{q}_A$ and $\boldsymbol{q}_F$ separately. Substituting (A4) back into (A2) and (A1), we obtain, at $\mathcal{O}(\epsilon)$, a linear eigenvalue problem for the unstable mode at $m = -1$,

$$\boldsymbol{L}_{-1}\boldsymbol{q}_A = i\boldsymbol{B}\omega_c\boldsymbol{q}_A, \tag{A5}$$

and a linear resolvent problem for the forced response at $m = m_f$,

$$(i\boldsymbol{B}\omega_f - \boldsymbol{L}_{m_f})\boldsymbol{q}_F = \boldsymbol{C}\boldsymbol{f}. \tag{A6}$$

We have denoted the linearised Navier–Stokes operator for the azimuthal mode m as $\boldsymbol{L}_m$ for brevity, i.e., $\boldsymbol{L}_m$ is the linear operator

$$\boldsymbol{L} = \left.\frac{\partial \boldsymbol{\mathcal{N}}}{\partial \boldsymbol{q}}\right|_{\boldsymbol{q}=\boldsymbol{q}_0}, \tag{A7}$$

where the θ-derivatives have been replaced with multiplications by im.

As $\boldsymbol{q}_2$ must balance the terms stemming from the quadratic non-linearities of $\boldsymbol{\mathcal{N}}(\cdot)$, we can see that it must have the form

$$\begin{aligned}\boldsymbol{q}_2(t,x,r,\theta) = \delta\boldsymbol{q}_\delta(x,r) + |A|^2\boldsymbol{q}_{A\bar{A}}(x,r) + |F|^2\boldsymbol{q}_{F\bar{F}}(x,r)\\ + (A^2\boldsymbol{q}_{AA}(x,r)e^{-2i\theta+2i\omega_c t} + AF\boldsymbol{q}_{AF}(x,r)e^{i(m_f-1)\theta+i(\omega_c+\omega_f)t}\\ + A\bar{F}\boldsymbol{q}_{A\bar{F}}(x,r)e^{-i(m_f+1)\theta+i(\omega_c-\omega_f)t} + F^2\boldsymbol{q}_{FF}e^{2im_f\theta+2i\omega_f t} + \text{c.c.}).\end{aligned} \tag{A8}$$

These terms are referred to as harmonics, if they have a nonzero temporal frequency, and as base-flow modifications, if they are steady. At $\mathcal{O}(\epsilon^2)$, the equations for each of these terms then read

$$-\boldsymbol{L}_0\boldsymbol{q}_\delta = -\boldsymbol{C}\nabla\cdot\boldsymbol{\tau}_0, \tag{A9}$$

$$-\boldsymbol{L}_0\boldsymbol{q}_{A\bar{A}} = -\boldsymbol{C}(\boldsymbol{u}_A\cdot\nabla_1\bar{\boldsymbol{u}}_A + \bar{\boldsymbol{u}}_A\cdot\nabla_{-1}\boldsymbol{u}_A), \tag{A10}$$

$$-\boldsymbol{L}_0\boldsymbol{q}_{F\bar{F}} = -\boldsymbol{C}(\boldsymbol{u}_F\cdot\nabla_{-m_f}\bar{\boldsymbol{u}}_F + \bar{\boldsymbol{u}}_F\cdot\nabla_{m_f}\boldsymbol{u}_F), \tag{A11}$$

$$(2i\boldsymbol{B}\omega_c - \boldsymbol{L}_{-2})\boldsymbol{q}_{AA} = -\boldsymbol{C}(\boldsymbol{u}_A\cdot\nabla_{-1}\boldsymbol{u}_A), \tag{A12}$$

$$(i\boldsymbol{B}(\omega_c+\omega_f) - \boldsymbol{L}_{m_f-1})\boldsymbol{q}_{AF} = -\boldsymbol{C}(\boldsymbol{u}_A\cdot\nabla_{m_f}\boldsymbol{u}_F + \boldsymbol{u}_F\cdot\nabla_{-1}\boldsymbol{u}_A), \tag{A13}$$

$$(i\boldsymbol{B}(\omega_c-\omega_f) - \boldsymbol{L}_{-m_f-1})\boldsymbol{q}_{A\bar{F}} = -\boldsymbol{C}(\boldsymbol{u}_A\cdot\nabla_{-m_f}\bar{\boldsymbol{u}}_F + \bar{\boldsymbol{u}}_F\cdot\nabla_{-1}\boldsymbol{u}_A). \tag{A14}$$

The notation ∇_m is used for the ∇ operator where, again, θ-derivatives are replaced with multiplications by im. We have also introduced the symbols $\boldsymbol{u}_X$ and $\boldsymbol{\tau}_X$ to represent the velocity field $\boldsymbol{u}$ and stress tensor $\boldsymbol{\tau}$ derived from the state $\boldsymbol{q}_X$.

Equation (A9) governs the correction to the base flow that arises from our slight supercriticality. The other harmonics and base-flow modifications are given by the resolvent problems (A10)-(A14) and represent the terms that stem from the non-linear interactions between the forcing, the unstable mode and their associated conjugates. In particular, $\boldsymbol{q}_{A\bar{A}}$ represents the base-flow modification caused by the unstable mode, $\boldsymbol{q}_{F\bar{F}}$ represents the base-flow modification caused by the forcing, $\boldsymbol{q}_{AA}$ represents the harmonic caused by the unstable mode interacting with itself, and $\boldsymbol{q}_{A\bar{F}}$ and $\boldsymbol{q}_{AF}$ represent the harmonics caused by the unstable mode interacting with the forcing.

In order to obtain an equation for the amplitude of the unstable mode, we assume that the amplitude A evolves on the slow time scale $T = \epsilon^2 t$, i.e., $A = A(T)$. This means that at $\mathcal{O}(\epsilon^3)$ we obtain

$$\boldsymbol{u}_A \frac{\mathrm{d}A}{\mathrm{d}T} = (\boldsymbol{\eta}\delta - |F|^2\boldsymbol{\mu})A - \boldsymbol{\nu}A|A|^2 \tag{A15}$$

where

$$\begin{aligned}\boldsymbol{\mu} = {} & \boldsymbol{u}_A \cdot \nabla_0 \boldsymbol{u}_{F\bar{F}} + \boldsymbol{u}_{F\bar{F}} \cdot \nabla_{-1}\boldsymbol{u}_A + \bar{\boldsymbol{u}}_F \cdot \nabla_{m_f-1}\boldsymbol{u}_{AF} + \boldsymbol{u}_{AF} \cdot \nabla_{-m_f}\bar{\boldsymbol{u}}_F + \\ & \boldsymbol{u}_F \cdot \nabla_{-(m_f+1)}\boldsymbol{u}_{A\bar{F}} + \boldsymbol{u}_{A\bar{F}} \cdot \nabla_{m_f}\boldsymbol{u}_F, \end{aligned} \tag{A16}$$

$$\boldsymbol{\eta} = -\left(\boldsymbol{u}_A \cdot \nabla_0 \boldsymbol{u}_\delta + \boldsymbol{u}_\delta \cdot \nabla_{-1}\boldsymbol{u}_A + \nabla_{-1} \cdot \boldsymbol{\tau}_A\right), \tag{A17}$$

$$\boldsymbol{\nu} = \boldsymbol{u}_A \cdot \nabla_0 \boldsymbol{u}_{A\bar{A}} + \boldsymbol{u}_{A\bar{A}} \cdot \nabla_{-1}\boldsymbol{u}_A + \bar{\boldsymbol{u}}_A \cdot \nabla_{-2}\boldsymbol{u}_{AA} + \boldsymbol{u}_{AA} \cdot \nabla_1 \bar{\boldsymbol{u}}_A. \tag{A18}$$

To reduce the vector equation (A15) to a scalar equation we take the inner product $\langle \cdot, \cdot \rangle$ of (A15) with $\boldsymbol{u}_A^\dagger$ where the state $\boldsymbol{q}_A^\dagger$ is given by the solution of the adjoint eigenvalue problem

$$\boldsymbol{L}_{-1}^\dagger \boldsymbol{q}_A^\dagger = -i\omega_c \boldsymbol{B}^\dagger \boldsymbol{q}_A^\dagger. \tag{A19}$$

The adjoint operator $\boldsymbol{L}_{-1}^\dagger$ is chosen so that the relation $\langle \boldsymbol{a}, \boldsymbol{L}_{-1}\boldsymbol{b}\rangle = \langle \boldsymbol{L}_{-1}^\dagger \boldsymbol{a}, \boldsymbol{b}\rangle$, is satisfied for all vectors $\boldsymbol{a}$ and $\boldsymbol{b}$. An analogous relation can be used to also obtain $\boldsymbol{B}^\dagger$. By choosing the adjoint eigenvector for the inner product, we ensure that we satisfy the Fredholm alternative and that the resulting scalar equation

$$\frac{\mathrm{d}A}{\mathrm{d}T} = \left(\eta\delta - |F|^2\mu)\right) A - \nu A|A|^2, \tag{A20}$$

has a unique solution [35]. The inner product used is

$$\langle \boldsymbol{a}, \boldsymbol{b}\rangle_c = \iint \boldsymbol{a}^H \boldsymbol{b}\, r\mathrm{d}r\mathrm{d}x, \tag{A21}$$

which is discretised to $\langle \boldsymbol{a}, \boldsymbol{b}\rangle_{\boldsymbol{W}} = \boldsymbol{a}^H \boldsymbol{W} \boldsymbol{b}$, with $\boldsymbol{W}$ as a positive definite weight matrix. As most of our vectors have no pressure component, we will use $\langle \boldsymbol{x}, \boldsymbol{y}\rangle$ to denote the inner product with the pressure component removed, where $\boldsymbol{x}$ and $\boldsymbol{y}$ have the same dimension as the velocity vector. We normalize the direct and adjoint eigenvectors such that $\langle \boldsymbol{u}_A, \boldsymbol{u}_A\rangle = 1$ and $\langle \boldsymbol{u}_A^\dagger, \boldsymbol{u}_A\rangle = 1$. The scalar coefficients in (5) are then obtained via $\mu = \langle \boldsymbol{u}_A^\dagger, \boldsymbol{\mu}\rangle$, $\eta = \langle \boldsymbol{u}_A^\dagger, \boldsymbol{\eta}\rangle$ and $\nu = \langle \boldsymbol{u}_A^\dagger, \boldsymbol{\nu}\rangle$.

2. Forcing with $m_f = 0$ and $\omega_f = 0$

For the case of $m_f = 0$ and $\omega_f = 0$, we use the asymptotic scaling $F' = \epsilon^2 F$, and search for solutions of the form

$$\begin{aligned}\boldsymbol{q} = \boldsymbol{q}_0 &+ \epsilon \left[A\boldsymbol{q}_A e^{-i\theta + i\omega_c t} + \text{c.c.}\right] \\ &+ \epsilon^2 \left[F\boldsymbol{q}_F + \delta \boldsymbol{q}_\delta + |A|^2 \boldsymbol{q}_{A\bar{A}} + \left(A^2 \boldsymbol{q}_{AA} e^{-2i\theta + 2i\omega_c t} + \text{c.c.}\right)\right],\end{aligned} \tag{A22}$$

where $-\boldsymbol{L}_0 \boldsymbol{q}_F = 2\boldsymbol{C}\boldsymbol{f}$. Following the analysis as before, we obtain a similar amplitude equation

$$\frac{\mathrm{d}A}{\mathrm{d}T} = (\eta\delta + F\mu)A - \nu A|A|^2, \tag{A23}$$

where the new forcing-dependent amplitude equation parameter is given by

$$\mu = -\left\langle \boldsymbol{u}_A^\dagger,\ \boldsymbol{u}_A \cdot \nabla_0 \boldsymbol{u}_F + \boldsymbol{u}_F \cdot \nabla_{-1} \boldsymbol{u}_A \right\rangle. \tag{A24}$$

As in the non-resonant case, the forcing can affect the linear growth rate of the mode. It is more efficient than harmonic forcing, though, as it acts at $O(\epsilon^2)$, and consequently, requires a smaller amplitude to have an effect. We can also see that as the forcing amplitude F appears rather than $|F|^2$, that we can obtain either a stabilising or destabilising effect depending on the sign of F.

3. Forcing with $m_f = -1$ and $\omega_f \approx \omega_c$

For near-resonant forcing with $m_f = -1$ and $\omega_f \approx \omega_c$, we use the scaling $F' = \epsilon^3 F$ and write the forcing frequency as $\omega_f = \omega_c + \Omega'$, in terms of the detuning parameter $\Omega' = \epsilon^2 \Omega$. We search for solutions of the form

$$\begin{aligned}\boldsymbol{q} = \boldsymbol{q}_0 &+ \epsilon \left[A\boldsymbol{q}_A e^{-i\theta + i\omega_c t} + \text{c.c.}\right] \\ &+ \epsilon^2 \left[\delta \boldsymbol{q}_\delta + |A|^2 \boldsymbol{q}_{A\bar{A}} + \left(A^2 \boldsymbol{q}_{AA} e^{-2i\theta + 2i\omega_c t} + \text{c.c.}\right)\right].\end{aligned} \tag{A25}$$

This leads to an amplitude equation with an external forcing term

$$\frac{\mathrm{d}A}{\mathrm{d}T} = \eta\delta A - \nu A|A|^2 + \mu F e^{i\Omega T}, \tag{A26}$$

with the forcing-dependent parameter $\mu = \langle \boldsymbol{u}_A^\dagger,\ \boldsymbol{f} \rangle$. The amplitude oscillates over the slow time scale. As the forcing amplitude increases, the flow responds at the forcing frequency, exhibiting 'lock-on'. The amplitude of forcing required is two orders of magnitude lower than in the non-resonant case.

4. Forcing with $m_f = -2$ and $\omega_f \approx 2\omega_c$

For near-resonant forcing with $m_f = -2$ and $\omega_f \approx 2\omega_c$, we use the scaling $F' = \epsilon^2 F$ and write the forcing frequency as $\omega_f = 2\omega_c + \Omega'$, in terms of the detuning parameter $\Omega' = \epsilon^2 \Omega$. We search for solutions of the form

$$\begin{aligned}\boldsymbol{q} = \boldsymbol{q}_0 &+ \epsilon \left[A \boldsymbol{q}_A e^{-i\theta + i\omega_c t} + \text{c.c.} \right] \\ &+ \epsilon^2 \left[\delta \boldsymbol{q}_\delta + |A|^2 \boldsymbol{q}_{A\bar{A}} + \left(A^2 \boldsymbol{q}_{AA} e^{-2i\theta + 2i\omega_c t} + \text{c.c.} \right) + \left(F \boldsymbol{q}_F e^{-2i\theta + 2i\omega_c t} + \text{c.c.} \right) \right]. \quad \text{(A27)}\end{aligned}$$

The amplitude equation has an external forcing term

$$\frac{\mathrm{d}A}{\mathrm{d}T} = \eta \delta A - \nu A |A|^2 + \mu F \bar{A} e^{i\Omega T}, \quad \text{(A28)}$$

where the forcing-dependent parameter is now given by

$$\mu = -\left\langle \boldsymbol{u}_A^\dagger,\ \boldsymbol{u}_F \cdot \nabla_1 \bar{\boldsymbol{u}}_A + \bar{\boldsymbol{u}}_A \cdot \nabla_{-2} \boldsymbol{u}_F \right\rangle. \quad \text{(A29)}$$

The amplitude of forcing required for 'lock-on' is one order of magnitude lower than in the non-resonant case.

Appendix B: Numerical convergence of parameters for different sized meshes and levels of grid refinement

This appendix lists the unstable eigenvalue as well as the amplitude equation parameters for $m_f = 0$ and $\omega_f = 1.3$. Three values of grid refinement parameter n_r are used as well as three different-sized domains, which have varying longitudinal and radial downstream boundary extents.

n_r	Our domain	Medium domain	Larger domain
1	$5.59 \times 10^{-5} + 2.092i$	$1.48 \times 10^{-3} + 2.094i$	$-3.34 \times 10^{-3} + 2.104i$
1.5	$-4.71 \times 10^{-6} + 2.096i$	$1.53 \times 10^{-3} + 2.095i$	$-3.57 \times 10^{-3} + 2.106i$
2	$-4.66 \times 10^{-4} + 2.100i$	$1.66 \times 10^{-3} + 2.095i$	$-3.57 \times 10^{-3} + 2.106i$

TABLE IV. The unstable mode for different domain sizes and mesh refinements. The larger domain has extent $r_{\text{outlet}} = 6$ and $x_{\text{outlet}} = 80$. The medium domain has extent $r_{\text{outlet}} = 4.5$ and $x_{\text{outlet}} = 60$.

n_r	μ	η	η
1	$-520.641 + 1028.15i$	$265.084 - 7.33649i$	$31.9202 + 32.9629i$
1.5	$-532.967 + 1039.68i$	$267.728 - 7.72871i$	$32.3236 + 33.1606i$
2	$-532.965 + 1033.51i$	$268.385 - 7.14049i$	$32.4255 + 32.9378i$

TABLE V. Convergence of equation parameters on the domain used for our results.

n_r	μ	η	η
1	$-522.859 + 1032.03i$	$269.482 - 13.669i$	$32.8235 + 33.0756i$
1.5	$-529.730 + 1042.77i$	$269.307 - 14.698i$	$32.3910 + 33.2808i$
2	$-534.125 + 1046.85i$	$270.752 - 15.713i$	$32.9828 + 33.4133i$

TABLE VI. Convergence of equation parameters on the medium domain.

n_r	μ	η	η
1	$-499.027 + 973.568i$	$267.631 - 1.00579i$	$31.8910 + 32.8924i$
1.5	$-508.404 + 982.173i$	$267.491 - 0.74688i$	$31.6760 + 32.7157i$
2	$-510.551 + 983.772i$	$268.079 - 1.78654i$	$32.2247 + 32.7137i$

TABLE VII. Convergence of equation parameters on the larger domain.

[1] Y. Huang and V. Yang, Dynamics and stability of lean-premixed swirl-stabilized combustion, Progress in Energy and Combustion Science **35**, 293 (2009).

[2] N. Syred, A review of oscillation mechanisms and the role of the precessing vortex core (pvc) in swirl combustion systems, Progress in Energy and Combustion Science **32**, 93 (2006).

[3] K. Oberleithner, M. Sieber, C. N. Nayeri, C. O. Paschereit, C. Petz, H.-C. Hege, B. R. Noack, and I. Wygnanski, Three-dimensional coherent structures in a swirling jet undergoing vortex breakdown: stability analysis and empirical mode construction, Journal of Fluid Mechanics **679**, 383 (2011).

[4] M. R. Ruith, P. Chen, E. Meiburg, and T. Maxworthy, Three-dimensional vortex breakdown in swirling jets and wakes: direct numerical simulation, Journal of Fluid Mechanics **486**, 331 (2003).

[5] H. Liang and T. Maxworthy, An experimental investigation of swirling jets, Journal of Fluid Mechanics **525**, 115 (2005).

[6] F. Gallaire, M. Ruith, E. Meiburg, J.-M. Chomaz, and P. Huerre, Spiral vortex breakdown as a global mode, Journal of Fluid Mechanics **549**, 71 (2006).

[7] J.-M. Chomaz, Global instabilities in spatially developing flows: non-normality and nonlinearity, Annual Review of Fluid Mechanics **37**, 357 (2005).

[8] F. Giannetti and P. Luchini, Structural sensitivity of the first instability of the cylinder wake, Journal of Fluid Mechanics **581**, 167 (2007).

[9] U. A. Qadri, D. Mistry, and M. P. Juniper, Structural sensitivity of spiral vortex breakdown, Journal of Fluid Mechanics **720**, 558 (2013).

[10] O. Tammisola and M. P. Juniper, Coherent structures in a swirl injector at re= 4800 by nonlinear simulations and linear global modes, Journal of Fluid Mechanics **792**, 620 (2016).

[11] T. L. Kaiser, T. Poinsot, and K. Oberleithner, Stability and sensitivity analysis of hydrodynamic instabilities in industrial swirled injection systems, Journal of Engineering for Gas Turbines and Power **140**, 051506 (2018).

[12] K. Oberleithner, M. Stöhr, S. H. Im, C. M. Arndt, and A. M. Steinberg, Formation and flame-induced suppression of the precessing vortex core in a swirl combustor: experiments and linear stability analysis, Combustion and Flame **162**, 3100 (2015).

[13] M. Stöhr, C. M. Arndt, and W. Meier, Transient effects of fuel–air mixing in a partially-premixed turbulent swirl flame, Proceedings of the Combustion Institute **35**, 3327 (2015).

[14] J. P. Moeck, J.-F. Bourgouin, D. Durox, T. Schuller, and S. Candel, Nonlinear interaction between a precessing vortex core and acoustic oscillations in a turbulent swirling flame, Combustion and Flame **159**, 2650 (2012).

[15] S. Terhaar, B. Ćosić, C. O. Paschereit, and K. Oberleithner, Suppression and excitation of the precessing vortex core by acoustic velocity fluctuations: An experimental and analytical study, Combustion and Flame **172**, 234 (2016).

[16] K. Oberleithner, M. Sieber, C. N. Nayeri, and C. O. Paschereit, On the control of global modes in swirling jet experiments, Journal of Physics: Conference Series **318**, 032050 (2011).

[17] P. Kuhn, J. P. Moeck, C. O. Paschereit, and K. Oberleithner, Control of the precessing vortex core by open and closed-loop forcing in the jet core, in *ASME Turbo Expo 2016: Turbomachinery Technical Conference and Exposition* (American Society of Mechanical Engineers, 2016) pp. V04BT04A036–V04BT04A036.

[18] F. Lückoff, M. Sieber, C. O. Paschereit, and K. Oberleithner, Characterization of different actuator designs for the control of the precessing vortex core in a swirl-stabilized combustor, Journal of Engineering for Gas Turbines and Power **140**, 041503 (2018).

[19] J. S. Müller, F. Lückoff, and K. Oberleithner, Guiding actuator designs for active flow control of the precessing vortex core by adjoint linear stability analysis, Journal of Engineering for Gas Turbines and Power **141**, 041028 (2019).

[20] O. Marquet, D. Sipp, and L. Jacquin, Sensitivity analysis and passive control of cylinder flow, Journal of Fluid Mechanics **615**, 221 (2008).

[21] U. A. Qadri and M. P. Juniper, A theoretical approach to the passive control of spiral vortex breakdown, in *Proceedings of 2012 UKACC International Conference on Control* (IEEE, 2012) pp. 656–661.

[22] U. A. Qadri, *Global stability and control of swirling jets and flames*, Ph.D. thesis, University of Cambridge (2014).

[23] S. Pasche, F. Gallaire, and F. Avellan, Predictive control of spiral vortex breakdown, Journal of Fluid Mechanics **842**, 58 (2018).

[24] D. Sipp and A. Lebedev, Global stability of base and mean flows: a general approach and its applications to cylinder and open cavity flows, Journal of Fluid Mechanics **593**, 333 (2007).

[25] P. Meliga, F. Gallaire, and J.-M. Chomaz, A weakly nonlinear mechanism for mode selection in swirling jets, Journal of Fluid Mechanics **699**, 216 (2012).

[26] D. Sipp, Open-loop control of cavity oscillations with harmonic forcings, Journal of Fluid Mechanics **708**, 439 (2012).

[27] X. Garnaud, L. Lesshafft, P. J. Schmid, and P. Huerre, Modal and transient dynamics of jet flows, Physics of Fluids **25**, 044103 (2013).

[28] X. Garnaud, L. Lesshafft, P. J. Schmid, and P. Huerre, The preferred mode of incompressible jets: linear frequency response analysis, Journal of Fluid Mechanics **716**, 189 (2013).

[29] U. A. Qadri and P. J. Schmid, Effect of nonlinearities on the frequency response of a round jet, Physical Review Fluids **2**, 043902 (2017).

[30] F. Hecht, New development in freefem++, J. Numer. Math. **20**, 251 (2012).

[31] G. Constantinescu and S. Lele, A highly accurate technique for the treatment of flow equations at the polar axis in cylindrical coordinates using series expansions, Journal of Computational Physics **183**, 165 (2002).

[32] C. S. Skene, *Adjoint based analysis for swirling and reacting flows*, Ph.D. thesis, Imperial College London (2019).

[33] D. Sipp and O. Marquet, Characterization of noise amplifiers with global singular modes: the case of the leading-edge flat-plate boundary layer, Theoretical and Computational Fluid Dynamics **27**, 617 (2013).

[34] C. S. Skene and P. J. Schmid, Adjoint-based parametric sensitivity analysis for swirling m-flames, Journal of Fluid Mechanics **859**, 516 (2019).

[35] P. J. Schmid and D. S. Henningson, *Stability and Transition in Shear Flows*, Applied Mathematical Sciences, Vol. 142 (Springer-Verlag, New York, NY, 2001).